The Astrophysical Journal Letters, 942:L1 (10pp), 2023 January 1 https://doi.org/10.3847/2041-8213/aca652
© 2022. The Author(s). Published by the American Astronomical Society.
OPEN ACCESS

The Identification of a Dusty Multiarm Spiral Galaxy at $z = 3.06$ with JWST and ALMA

Yunjing Wu[1,2], Zheng Cai[1], Fengwu Sun[2], Fuyan Bian[3], Xiaojing Lin[1], Zihao Li[1], Mingyu Li[1], Franz E. Bauer[4,5], Eiichi Egami[2], Xiaohui Fan[2], Jorge González-López[6,7], Jianan Li[1], Feige Wang[2,8], Jinyi Yang[2,9], Shiwu Zhang[1], and Siwei Zou[1]
[1] Department of Astronomy, Tsinghua University, Beijing 100084, People's Republic of China; zcai@mail.tsinghua.edu.cn
[2] Steward Observatory, University of Arizona, 933 N Cherry Ave, Tucson, AZ 85721, USA
[3] European Southern Observatory, Alonso de Córdova 3107, Casilla 19001, Vitacura, Santiago 19, Chile
[4] Instituto de Astrofisica, Facultad de Fisica, Pontificia Universidad Catolica de Chile Av. Vicuna Mackenna 4860, 782-0436 Macul, Santiago, Chile
[5] Millennium Institute of Astrophysics, Nuncio Monseñor Sótero Sanz 100, Providencia, Santiago, Chile
[6] Las Campanas Observatory, Carnegie Institution of Washington, Casilla 601, La Serena, Chile
[7] Núcleo de Astronomía de la Facultad de Ingeniería y Ciencias, Universidad Diego Portales, Av. Ejército Libertador 441, Santiago, Chile
Received 2022 October 4; revised 2022 November 21; accepted 2022 November 23; published 2022 December 27

Abstract

Spiral arms serve crucial purposes in star formation and galaxy evolution. In this paper, we report the identification of "A2744-DSG-z3," a dusty, multiarm spiral galaxy at $z = 3.059$ using the James Webb Space Telescope (JWST) NIRISS imaging and grism spectroscopy. A2744-DSG-z3 was discovered as a gravitationally lensed submillimeter galaxy with the Atacama Large Millimeter/submillimeter Array (ALMA). This is the most distant stellar spiral structure seen thus far, consistent with cosmological simulations that suggest $z \approx 3$ as the epoch when spirals emerge. Thanks to the gravitational lensing and excellent spatial resolution of JWST, the spiral arms are resolved with a spatial resolution of ≈290 pc. Based on spectral energy distribution fitting, the spiral galaxy has a delensed star formation rate of $85 \pm 30\ M_{\odot}\ \mathrm{yr}^{-1}$, and a stellar mass of $\approx 10^{10.6}\ M_{\odot}$, indicating that A2744-DSG-z3 is a main-sequence galaxy. After fitting the spiral arms, we find a stellar effective radius ($R_{\mathrm{e,star}}$) of 5.0 ± 1.5 kpc. Combining with ALMA measurements, we find that the effective radii ratio between dust and stars is ≈0.4, similar to those of massive star-forming galaxies (SFGs) at $z \sim 2$, indicating a compact dusty core in A2744-DSG-z3. Moreover, this galaxy appears to be living in a group environment: including A2744-DSG-z3, at least three galaxies at $z = 3.05$–3.06 are spectroscopically confirmed by JWST/NIRISS and ALMA, residing within a lensing-corrected projected scale of ≈70 kpc. This, along with the asymmetric brightness profile, further suggests that the spiral arms may be triggered by minor-merger events at $z \gtrsim 3$.

Unified Astronomy Thesaurus concepts: Spiral galaxies (1560)

1. Introduction

Spiral structures are common among galaxies in the local universe. Some exhibit grand design morphology, in which prominent and well-defined spiral arms can be determined, while other galaxies show multiarm or flocculent spirals, with subtler structural features (Elmegreen et al. 2011; Elmegreen & Elmegreen 2014). Extensive efforts have been conducted to investigate the morphology, to understand the spiral/disk formation mechanism, and to study the relation between the spiral and star formation (e.g., Lin & Shu 1964; Conselice 2014). Nevertheless, when and how large spirals emerged in the early universe is largely unknown.

Several studies have been conducted to search for spiral structures at $z \gtrsim 2$, the peak of cosmic star formation, and to study the initial formation and evolution of the spiral morphology (e.g., Chen et al. 2022; Fudamoto et al. 2022; Margalef-Bentabol et al. 2022). With the Atacama Large Millimeter/submillimeter Array (ALMA), Tsukui & Iguchi (2021) discovered a cold, [C II]-emitting rotating gaseous disk that can be interpreted as either spiral arms or tidal structures. Nevertheless, the stellar spiral structures are even rarer at high-z universe. Only a small number of stellar spiral structures are identified at $z > 2$ that have been spectroscopically confirmed, including HDFX 28 at $z = 2.011$ (Dawson et al. 2003), Q2343-BX442 at $z = 2.18$ (Law et al. 2012), and RS14, which is recently shown by James Webb Space Telescope (JWST) observations at $z = 2.46$ (Fudamoto et al. 2022). No stellar spiral structure has yet been confirmed at $z > 3$.

Currently, it is still unclear whether the rare appearance of spirals at high z is mainly due to the spiral formation or surface brightness dimming. At $z > 2$, galaxies are observed to be clumpier and more irregular (e.g., Elmegreen et al. 2009). Law et al. (2009) suggest that the irregularity at $z \gtrsim 2$ can be explained, because the disks could be dynamically hot, and hot disks could yield more clumps than spiral structures (Conselice et al. 2005). Simulations further suggest that clumpy galaxies may transition into spirals. Nevertheless, at high z, direct observational constraints linking gaseous clumps and spirals are lacking, while our understanding of how spirals may impact star formation remains unclear. For example, whether spirals at $z > 2$ can enhance the star formation or not are still under debated (e.g., Elmegreen 2002; Moore et al. 2012). All these questions or debates can be addressed by identification of more spirals across cosmic time and studying their star formation properties. Such observations can also answer the long-standing question of when and where spiral structures start to emerge in the early universe, as well as what their evolutionary endpoints at present time might be.

[8] NHFP Hubble Fellow.
[9] Strittmatter Fellow.

Original content from this work may be used under the terms of the Creative Commons Attribution 4.0 licence. Any further distribution of this work must maintain attribution to the author(s) and the title of the work, journal citation and DOI.

Table 1
Physical Properties of A2744-DSG-z3

Galaxy	A2744-DSG-z3
R.A. (deg)	3.58502
Decl. (deg)	–30.38181
$z_{\rm spec}$	3.059
μ	2.45
Physical parameters	
Inclination (deg)	28
Pitch angle (deg)	34 ± 13
Hubble type	Sc
SFR ($M_\odot$ yr^{-1})[a]	85 ± 30
$\log[M_{\rm star}/(M_\odot)]$	10.55
$\log[M_{\rm dust}/(\mu^{-1}M_\odot)]$[a]	8.70 ± 0.10
$R_{\rm e,star}$ (kpc)	5.0 ± 1.5
$R_{\rm e,dust}$ (kpc)[b]	2.04 ± 0.26

Notes.
[a] Reference of SFR and dust mass is from Sun et al. (2022),
[b] Delensed result. Reference of effective radius of dust continuum: F. Sun et al. (2022, in preparation).

In this paper, we present our identification of a stellar spiral at $z > 3$. This galaxy is reported as a submillimeter galaxy (SMG) with the ALMA Frontier Field survey (González-López et al. 2017; Laporte et al. 2017), and recovered recently with the ALMA Lensing Cluster Survey (ALCS; Sun et al. 2022) with updated spectroscopic redshift $z = 3.06$. Nevertheless, ALMA spatial resolution ($\approx 0\farcs6$–$1\farcs0$) is insufficient to resolve most spiral-like structures for galaxies at $z \gtrsim 3$. JWST has a near-infrared capability that allows us to probe the stellar properties of high-z galaxies. The high spatial resolution ($\approx 0\farcs06$) enables us to fully resolve the spiral structures. We named this galaxy as A2744-DSG-z3 in the following of the paper, where DSG is the acronym of "dusty spiral galaxy."

This paper is organized as follows: Section 2 describes details of data and reduction technique. Section 3 presents the spectra of A2744-DSG-z3 obtained from ALMA and JWST/NIRISS and a stellar-mass surface density map. In Section 4, we provide further discussion of our observations. In this paper, we assume a flat cosmological model with $\Omega_M = 0.3$, $\Omega_\Lambda = 0.7$ and $H_0 = 70\,{\rm km\,s^{-1}\,Mpc^{-1}}$, $1'' = 7.7$ kpc at $z = 3.06$. The Glafic lensing model is adopted (Oguri 2010).

2. Data

2.1. JWST/NIRISS Imaging and Grism Observations

The NIRISS data were obtained from the GLASS JWST Early Release Science Program (Treu et al. 2022) with direct imaging in F115W, F150W, and F200W and grism spectroscopic observations. The direct-imaging exposure time is 2834.504 s $\simeq$ 0.79 hr per each band. The data were reduced using the standard JWST pipeline[10] v1.6.2 with calibration reference files "`jwst_0944.pmap`." $1/f$ noise (see Schlawin et al. 2020) was modeled and removed using the code `tshirt`,[11] and the "snowball" artifacts from cosmic rays (Rigby et al. 2022) were identified and masked. The world coordinate system of mosaicked images were registered using the Pan-STARRS1 catalog (Flewelling et al. 2020). The pixel scale of final mosaicked images is resampled to $0\farcs03$ with `pixfrac` = 0.8.

We reduced the grism data using GRIZLI[12] (Version 1.6, Brammer 2022). The 2D grism spectra were drizzled using a pixel scale $0\farcs065$. The contamination was subtracted by forward modeling of the full field-of-view (FOV) grism images. We derived reliable spectroscopic redshifts via spectral template fitting based on a library of spectral energy distributions (SEDs).

2.2. ALMA CO Observations and the Determination of Redshift

Band 3 and 4 line-scan observations of our target are available in the ALMA archive (Program 2017.1.01219.S; PI: Bauer). The frequency ranges from 84.10–99.97 to 139.51–155.38 GHz, covering CO (3–2) and (5–4) emission lines (rest-frame: 345.7960/576.2679 GHz) at $z = 3.06$ as reported in Sun et al. (2022). The on-source time of these observations is 12.5 and 10.0 minutes. The spectra were directly extracted by rebinning the channel width to 74/69 km s^{-1} for CO(3–2) and CO(5–4) of available data products, using the CASA package v6.3.0 (McMullin et al. 2007).

3. Analysis and Results

In this Letter, we focus on the physical properties of A2744-DSG-z3. Detailed information is listed in Table 1. Figure 1 shows the color composite map of this target. We note that there are two companion galaxies in the same field that could be related to A2744-DSG-z3. The first one is a star-forming dwarf galaxy close to A2744-DSG-z3, denoted as GLASS-Z grad1 (Wang et al. 2022). The angular offset is $\approx 3\farcs1$ on the image plane and then is delensed to $\approx 2''$. The second companion galaxy is on the southwest side of A2744-DSG-z3. The observed angular separation is $\approx 15''$, corresponding to a lensing-reconstructed impact parameter of $\approx 9\farcs6$ (i.e., $\approx$74 kpc at $z = 3$; M. Li et al. 2022, in preparation). The redshift of A2744-DSG-z3 is determined by ALMA CO observations (see the left panel of Figure 2). The redshifts of two companion galaxies are confirmed by the JWST/NIRISS [O III]/Hβ spectroscopy. The right panel of Figure 2 shows the extracted 1D/2D grism spectra of A2744-DSG-z3. The grism spectra do not show obvious emission lines, while the 4000 Å break is tentatively detected in F150W band. The best-fit redshift based on the grism spectra provided by GRIZLI is consistent with that determined by ALMA (see the probability density distribution in Figure 2).

3.1. Size Ratio between Dust and Stellar Components

Dust in the central few kpc region is likely generated by a central starburst, favoring an inside-out star-forming scenario (Nelson et al. 2016; Tadaki et al. 2020). Meanwhile, the rest-frame optical continua allows to probe the galaxy-scale star formation (Gullberg et al. 2019). Thus, the dust-to-stellar effective radius ratio ($R_{\rm e,dust}/R_{\rm e,star}$) reflects the comparison between two-component star formation models (Lang et al. 2019; Tadaki et al. 2020; Sun et al. 2021). This dusty spiral galaxy, A2744-DSG-z3, provides us the opportunity to connect the intense star formation process and the structure formation of spiral arms and bulges.

[10] https://github.com/spacetelescope/jwst
[11] https://github.com/eas342/tshirt
[12] https://github.com/gbrammer/grizli/

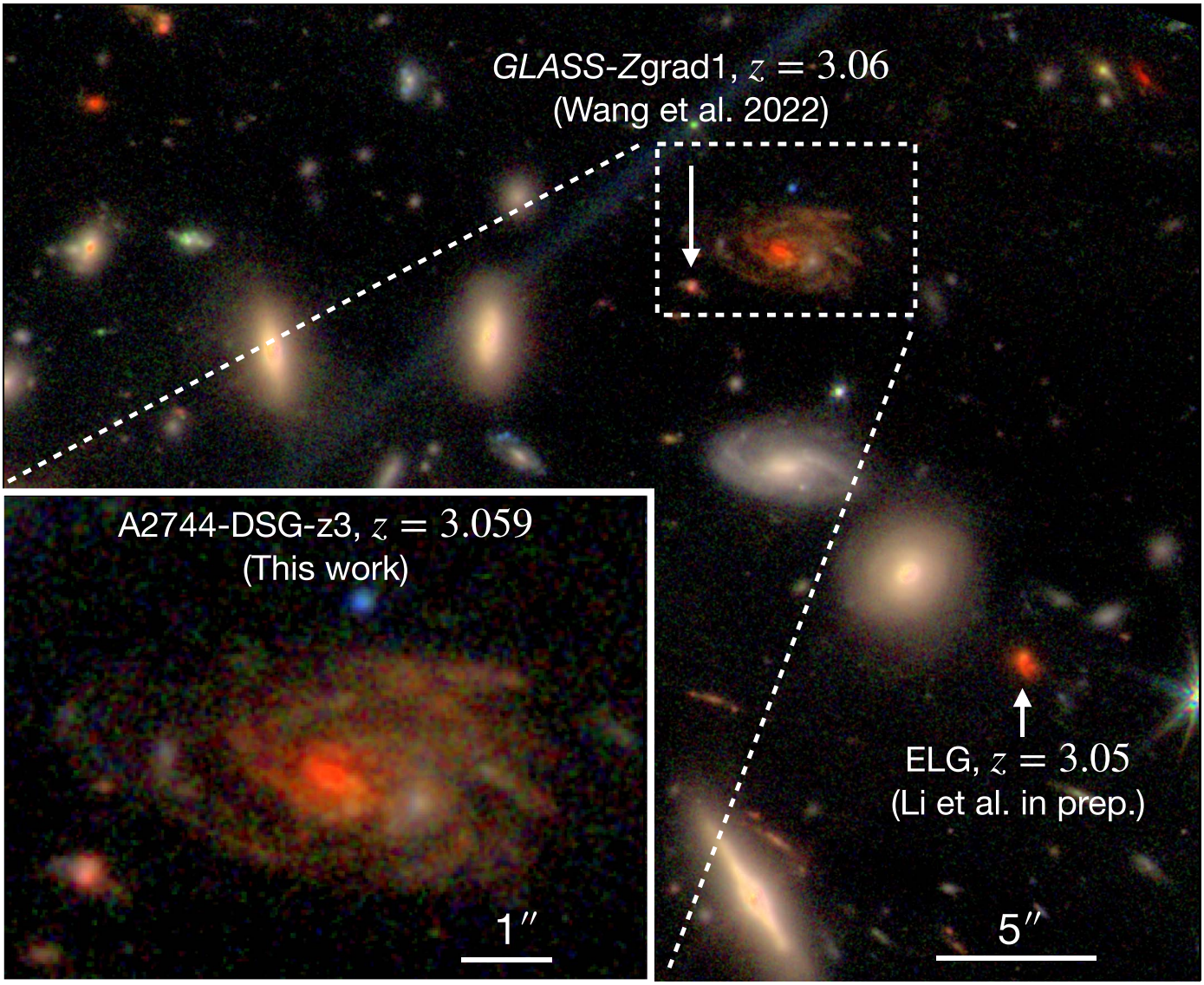

Figure 1. Dusty spiral galaxy (DSG) at $z = 3.059$. The composite RGB map of the target A2744-DSG-z3 is based on 3-band JWST/NIRISS imaging observations with pixel scale of $0\farcs03$ (blue: F115W, green: F150W, red: F200W). The target A2744-DSG-z3 was initially reported by the ALMA Frontier Fields survey (González-López et al. 2017; Laporte et al. 2017, A2744-ID03 in their papers) as an SMG (see also Sun et al. 2022). Meanwhile, the target GLASS-Z grad1, reported in Wang et al. (2022), is a star-forming galaxy with stellar mass (M_*) of $\sim 10^9 M_\odot$ at the same redshift. The impact parameter between these two galaxies is $\approx 3\farcs1$. Another emission-line galaxy is confirmed by NIRISS grism and ALMA as well at $z = 3.05$ (M. Li et al. 2022, in preparation) with the projected separation of $15''$. This galaxy was also reported as an SMG with $M_{\rm dust} \simeq 10^{8.6} M_\odot$ (Laporte et al. 2017; Sun et al. 2022).

To investigate the stellar component, we used reconstructed broadband imaging observations that trace the rest-frame optical emission of A2744-DSG-z3. However, for star-forming galaxies, the size measured from the stellar-density map would be more compact than that observed from surface brightness, which is due to the surface brightness dimming effects (Wuyts et al. 2012; Genzel et al. 2020). Therefore, measuring half-light radius would overestimate the size of stellar mass. Fortunately, there is a strong empirical relation between stellar mass-to-light ($M_{\rm star}/L$) ratio and the optical colors for spiral galaxies (e.g., Bell & de Jong 2001).

Following Lang et al. (2019), we derived the stellar mass based on broadband color ($J_{115} - K_{200}$). Our photometric process is listed as follows. First, we matched point-spread functions (PSFs). To construct PSFs in different filters, we selected stars from Gaia DR3 archival catalog (Gaia Collaboration et al. 2016, 2022) and then stacked unsaturated ones in the FOV. After matching PSFs to that of F200W, we performed pixel–pixel photometry in both J_{115} and K_{200} bands. The photometric zero-points are determined using the calibration file "`jwst_niriss_photom_0028.rmap`." The K-band observations and color maps are shown in the left two panels of Figure 3. In Figure 3, the spiral associated pixels were identified with the flux density over 2σ noise (determined by the pixel-to-pixel standard deviation). Here, we note that there could be a foreground target that could contaminate A2744-DSG-z3 (see Appendix A). Thus, we masked it before performing measurements.

We then obtained the stellar-mass density ($\Sigma_{M_{\rm star}}$) map based on the relation between mass-to-light ratio and color. This relation was constructed and calibrated using simulated SEDs derived from stellar population synthesis methods (see

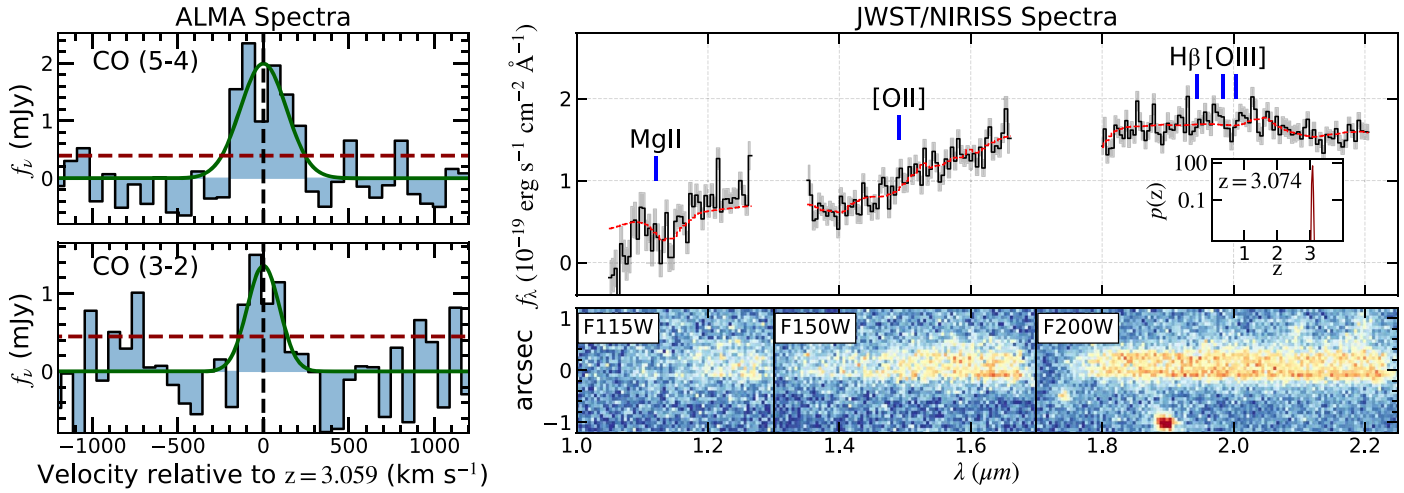

Figure 2. Determinations of the redshift of DSG-z3. Left: ALMA CO (5–4) and (3–2) spectra of A2744-DSG-z3. The dashed red line shows 1σ noise spectra, while the dashed black line represents the systemic velocity. Dark-green curves show the best-fit Gaussian models of the spectra, indicating the CO-based redshift of $z_{\rm CO} = 3.059 \pm 0.001$. Right: top panel shows the optimally extracted 1D spectra from NIRISS 3-band grism observations. Black histogram denotes the observed flux density, with gray shadows showing 1σ errors. The dashed red lines are the GRIZLI modeled spectra containing continuum and nebular emission templates obtained by best SED fitting. The vertical blue lines mark the location of common emission lines ([O III], Hβ, [O II], and Mg II) that are not detected in DSG-z3. The subplot at bottom right shows the probability distribution function of redshifts from SED fitting, indicating that the best grism redshift of this target is $z \approx 3.07$. Bottom panels are the joint 2D spectra covered by NIRISS three filters (F115W, F150W, and F200W).

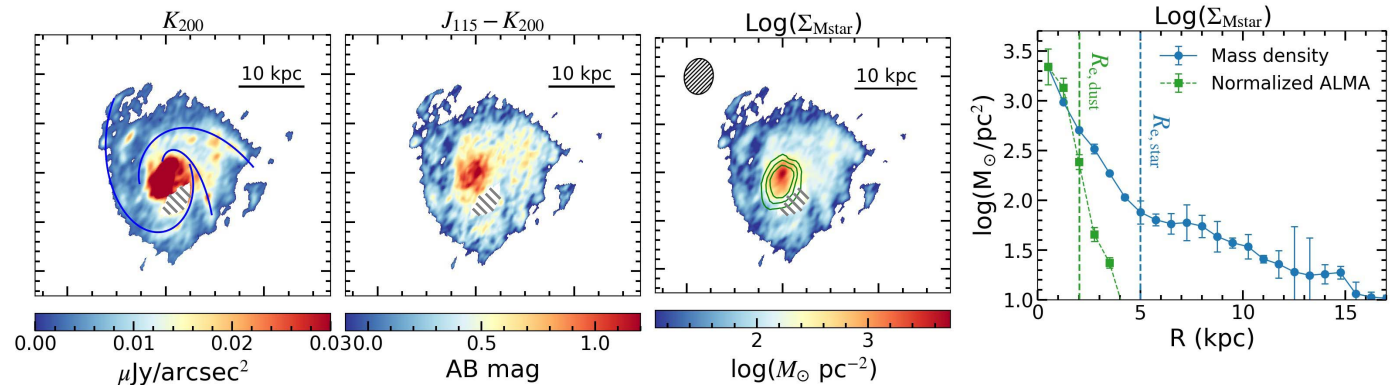

Figure 3. From left to right: reconstructed K_{200}-band cutout map, $J_{115} - K_{200}$ color map, stellar surface density map, and lensing-corrected stellar-density/dust-continuum radial profile. Pixels belonging to A2744-DSG-z3 with fluxes higher than 2σ (determined by the pixel–pixel standard deviation) were shown. The stellar-mass surface density map is derived based on a best-fit $M_{\rm star}/L$ vs. color relation. In the K_{200}-band map (Left panel), blue lines represent spiral arms fitted by the Logarithmic spirals equation (see Section 3.1, Equation (2)). Additionally, the ALMA dust-continuum observations are shown in the stellar surface density map (the third panel) as green contours ranging from [5, 7.5, 10] $\times \sigma$. In the right panel, we obtained the effective radius of stellar mass and dust continuum from the observed radial profile, i.e., $R_{\rm e,star} = 5.0 \pm 1.5$ kpc, $R_{\rm e,dust} = 2.04 \pm 0.26$ kpc. Tentative foreground interloper is masked as gray lines.

Appendix B). The best-fit relation is

$$M_{\rm star}/L = 0.55 \times (J_{115} - K_{200}) + 18.92, \quad (1)$$

where the mass and luminosity are in solar units. We then obtained the pixelated $\Sigma_{M_{\rm star}}$ map (third panel of Figure 3) with the $M_{\rm star}/L$–color relation above. We measured the radial profile of stellar surface density by averaging it in the deprojected galactocentric plane with the radial interval of 1 kpc (see the last panel of Figure 3). The major axis of the galaxy was determined by the second-order moments of its stellar-mass distribution relative to its mass density peak (Chen et al. 2021). The $R_{\rm e,star}$, defined as the radius containing half the mass, was calculated from the $\Sigma_{M_{\rm star}}$ profile. The measured $R_{\rm e,star}$ is 5.0 ± 1.5 kpc. We note that the $R_{\rm e,star}$ was calculated by numerically integrating the mass density profile out to 17 kpc, approaching the outskirt of the disk.

The effective radius of the dust continuum at a rest-frame wavelength of 280 μm was measured using ALMA Band 6 data (2018.1.00035.L, PI: Kohno) through a UV-plane visibility profile modeling. The best-fit circularized effective radius assuming a Gaussian profile is $R_{\rm e,dust} = 0\farcs42 \pm 0\farcs05$, corresponding to a physical size of 2.04 ± 0.26 kpc after correcting for lensing magnification. This is consistent with the size derived assuming an exponential profile ($0\farcs39 \pm 0\farcs07$), and the detailed methodology will be presented by F. Sun et al. (2022, in preparation) among a larger sample of lensed dusty star-forming galaxies discovered with the ALCS (Sun et al. 2022). We conclude here that the measured radius ratio of A2744-DSG-z3 is $R_{\rm e,dust}/R_{\rm e,star} = 0.41 \pm 0.13$. We also note that detailed CO kinematic information is provided in the Appendix C.

Furthermore, we measure the physical parameters of the observed spiral-arm like features. Following Law et al. (2012), we used the Logarithmic spiral equation (Davis et al. 2012):

$$r = r_0 e^{\theta \tan(\phi)}, \quad (2)$$

where r, r_0, θ, and ϕ represent the radius, initial radius, angle, and pitch angle of arms, respectively. In the NIRISS-F200W imaging data, there are three spiral arms flowing into the red bulge. Thus, considering inclination effects, we fit their shape using Equation (2). The best-fit results (blue lines in the left panel of Figure 3) show that the logarithmic equation effectively reproduces the arms. The best-fit pitch angle of the arms is $\phi = 34° \pm 13°$, similar to that of the three-armed spiral galaxy at $z = 2.18$ (Law et al. 2012).

4. Discussion

4.1. Implication of the Observed Dust-to-stellar-radius Ratio

Smaller dust-to-stellar-radius ratio ($R_{\rm e,dust}/R_{\rm e,star}$) indicates more compact dust emission, which is possibly caused by a gas-rich merger and more active star formation (Nelson et al. 2016; Tacchella et al. 2016; Gullberg et al. 2019). In contrast, larger $R_{\rm e,dust}/R_{\rm e,star}$ ratio corresponds to relatively weak star formation (Tadaki et al. 2020; Sun et al. 2021). To analyze the star-forming and structural properties, following Tadaki et al. (2020) and Sun et al. (2021), we compare the main-sequence offset (ΔMS) and the dust-to-stellar size ratio with those of dusty star-forming galaxies at $z \sim 2$. ΔMS is defined as the star formation rate (SFR) ratio between the observed value and that expected on the so-called star-forming "main sequence" ($\rm SFR_{MS}$), i.e., $\Delta{\rm MS} = \log[{\rm SFR}/{\rm SFR_{MS}}]$ (Speagle et al. 2014). The observed SFR of A2744-DSG-z3 is $\log[{\rm SFR}_{\rm obs}/(\mu^{-1} M_\odot\,{\rm yr}^{-1})] = 2.32 \pm 0.16$ derived by SED-fitting results and reported in Sun et al. (2022). We follow Speagle et al. (2014) to calculate the $\rm SFR_{MS}$ ($\rm SFR_{MS} = SFR_{MS}(M_{star}, z)$), using the stellar mass of A2744-DSG-z3 by summing up the delensed stellar-mass density map, which is $\log(M_{\rm star}/M_\odot) = 10.55$. With an estimated main-sequence SFR of $\log[{\rm SFR_{MS}}/(M_\odot\,{\rm yr}^{-1})]$ of $\approx$2.01 (delensed), the intrinsic ΔMS of A2744-DSG-z3 is ≈ -0.08.

We compare our size measurements with those of dusty star-forming galaxies at $z \sim 2$ (Lang et al. 2019; Tadaki et al. 2020) in Figure 4. The average $R_{\rm e,dust}/R_{\rm e,star}$ of SMGs is 0.6 ± 0.2 (blue shaded region in Figure 4; Lang et al. 2019), suggesting that the distribution of dust components is more compact than the stellar ones (see also Hodge et al. 2016; Sun et al. 2021; Gómez-Guijarro et al. 2022). This result is also consistent with that observed from massive star-forming galaxies (blue dots in Figure 4; Tadaki et al. 2020). As an SMG, the observed radius ratio (0.41) of A2744-DSG-z3 is broadly consistent with SMGs in previous studies, but smaller than those of local spirals ($R_{\rm e,dust}/R_{\rm e,star} \approx 1$; Hunt et al. 2015; Bolatto et al. 2017). Given the observed ΔMS (-0.08), our results suggest that, as a spiral galaxy, A2744-DSG-z3 is on the star-forming main sequence ($-0.4 < \Delta{\rm MS} < 0.4$), similar to local spirals that are also on the main sequence. However, A2744-DSG-z3 hosts a more compact dust core than those of local spirals while consistent with the majority of SMGs at $z \approx 2$ (Figure 4).

The majority of observed SFR of A2744-DSG-z3 at the current epoch is obscured and traced by the compact FIR emission at the center core region ($R_{\rm e,dust} \approx 2$ kpc), further surrounded by a more extended stellar disk ($\approx$5 kpc). The observed dusty core size ($\approx$2 kpc) of A2744-DSG-z3 is comparable to the typical galactic bulge size ($\approx$1 kpc) for galaxies with stellar mass of $\sim 10^{11} M_\odot$ at $z \sim 2$ (Tadaki et al. 2017). The observed star formation at the bulge scale suggests an active bulge formation scenario. After the quenching of the compact dusty star formation in the core of A2744-DSG-z3, a compact stellar component will remain in the center of the galaxy as the newly formed bulge.

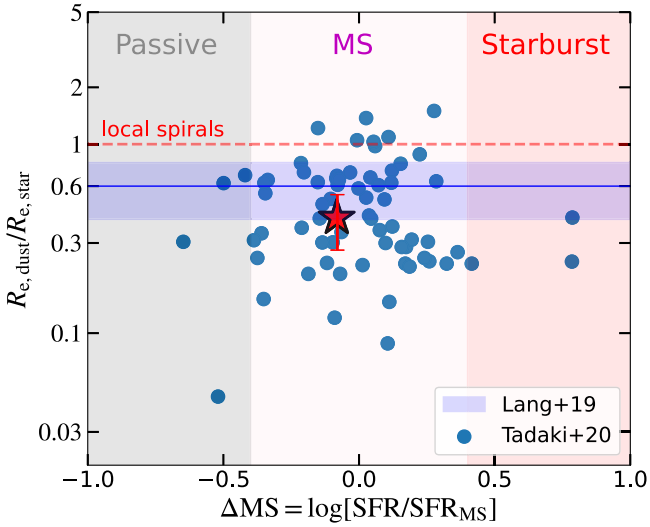

Figure 4. Dust and stellar effective radius ratio vs. main-sequence offset (ΔMS). Blue dots are massive SFGs at $z \sim 2$ reported by Tadaki et al. (2020), while the red star represents the results of A2744-DSG-z3. Shaded blue region indicates the radius ratio observed of SMGs at $z \sim 2$ (Lang et al. 2019). ΔMS is defined as SFR ratios between the observed value and the expected ones on the star-forming MS. Following Aravena et al. (2020), the boundaries between passive, main-sequence, and starburst galaxies are distinguished by $\Delta{\rm MS} = \pm 0.4$, respectively. We conclude that, the spiral galaxy, A2744-DSG-z3, has a more compact dust core compared with SMGs at $z \sim 2$ and local spirals. And the star-forming intensity is the same as main-sequence galaxies at $z = 3$. Our observations suggest that for A2744-DSG-z3 at $z = 3$, the bulge was formed with star formation at the center core region ($\lesssim$2 kpc).

4.2. Group Environment and the Formation of Spiral-like Structure at $z \gtrsim 3$

Thanks to the JWST/NIRISS grism observations, the target close to A2744-DSG-z3 (GLASS-Zgrad1, recently reported in Wang et al. 2022) is identified as one companion galaxy at the same redshift. The stellar mass of GLASS-Zgrad1 is $\approx 10^9\,M_\odot$, and the delensed angular separation between the two sources is $\approx 2''$, corresponding to 15.4 kpc at $z = 3.06$. The stellar mass of A2744-DSG-z3 is $\approx 10^{10.6} M_\odot$, suggesting a halo mass of $\sim 10^{12.5}\,M_\odot$ (Rodríguez-Puebla et al. 2017; Somerville et al. 2018) with a Virial radius of $\sim$120 kpc.[13] The lensing-corrected projected separation between these two galaxies reside within the Virial radius. With the mass ratio between these two galaxies being $\approx$36, this implies a minor-merger interaction scenario that potentially triggered the dusty central starburst in A2744-DSG-z3. Law et al. (2012) also suggest that one spiral galaxy at $z \sim 2$ could be formed by the minor-merger process.

We note that, in the field A2744, Boyett et al. (2022) reported a number counts excess at $z \sim 3$. Thus, A2744-DSG-z3 could reside in an overdense region. For the companion galaxy, GLASS-Zgrad1, the measured slope in the metallicity distribution is $\Delta \log({\rm O/H})/\Delta r = 0.165 \pm 0.022$ (Wang et al. 2022). The occurrence of inverted gradients measured in this galaxy could also be explained by an ongoing minor merger. Due to the loss of angular momentum by the torque in the

[13] https://github.com/ylu2010/DarkMatterHaloCalculator

merger interactions, the metal-poor gas inflows into the inner disk to flatten/invert the metallicity gradient (Krabbe et al. 2011). Alternatively, the group environment may also give rise to enhanced cold mode accretion on the member galaxies, which inverts the metal gradient (Li et al. 2022).

To understand the environmental influence on the spiral formation, first, we note that the stellar spiral in A2744-DSG-z3 is present at $z = 3.06$, just around the peak of cosmic star formation (see Madau & Dickinson 2014 for a review). Thus, the number of galaxies and merger rates could be high. Cosmological simulations suggest that high-redshift spiral structures may be caused by higher merger rate (Hammer et al. 2009), high inflow rate, and the low angular momentum of cold streams (Cen 2014). Meanwhile, there are simulations reporting that the spirals exist by $z \approx 3$ (Fiacconi et al. 2015) and the high-redshift spirals may be arisen from swing amplifications triggered by galaxy interactions. Kohandel et al. (2019) further showed that the cold gaseous spiral structure (close to the reionization epoch) can exist when the galactic disk is relaxed after a merger. A2744-DSG-z3 could experience a merger-like process; and this could enhance the formation of spirals as predicted by cosmological simulations.

5. Summary

In this Letter, we present the first identification of a dusty spiral galaxy (A2744-DSG-z3) at $z = 3.059$ observed by ALMA and JWST/NIRISS in both slitless-spectroscopic and direct-imaging modes. The redshift of A2744-DSG-z3 is determined through ALMA CO observations. Meanwhile, by fitting the rest-frame optical continuum spectra provided by the NIRISS/grism using GRIZLI, we also obtained a redshift solution of A2744-DSG-z3 with $z \approx 3.07$, consistent with that obtained from ALMA observations. The best-fit three spiral-arm models to the NIRISS/F200W direct images suggests an inclination/pitch angle of 28 (deg) and 34 ± 13 (deg), respectively. We convert the observed F115W − F200W colors and flux densities to stellar masses, and find a stellar-mass effective radius of 5.0 kpc, while the effective dust radius is 2.04 ± 0.26 kpc. Furthermore, the NIRISS grism data also identify a companion dwarf galaxy, called *GLASS-Z*grad1 (Wang et al. 2022), with the projected separation of 15.4 kpc (delensed). The identification of this galaxy pair suggests a minor-merger scenario that triggers the dusty central starburst in A2744-DSG-z3.

The high-spatial-resolution imaging observations provided by JWST give us the first opportunity to resolve the detailed structure of a spiral galaxy at $z \sim 3$ to a physical scale of ≈290 pc. Additionally, the NIRISS grism spectroscopic observations provides us the chance to determine redshifts for bright targets or emitters within a sky coverage of $\sim 2'$. Like the galaxy pair identified in this work, spectroscopic redshifts through emission lines will further help us to investigate the environments of galaxies at different redshifts.

The observed dust versus stellar component radius ratio (0.41) of A2744-DSG-z3 suggests that the dust core is more compact than that observed of local spirals (≈1). The observed main-sequence offset (−0.08) indicates that this target is undergoing the same intense star formation activities as main-sequence galaxies at $z = 3$. Furthermore, A possible minor-merger scenario may help to explain the observed inverted metallicity gradient of GLASS-Zgrad1 due to the interaction. We note that, future high-spatial-resolution observations (e.g., ALMA CO for A2744-DSG-z3 and JWST/NIRSpec-IFU for GLASS-Zgrad1) will allow to probe the dynamics of this minor-merger candidate.

Y.W. thanks Shude Mao, Jerry Sellwood, Zuyi Chen, and Xin Wang and for very helpful discussions. We thank the anonymous referee for reading the paper carefully and providing comments that helped improve and strengthen this paper. Z.C., Y.W., X.L., Z.L., M.L., J.L., and S.Z. are supported by the National Key R&D Program of China (grant No. 2018YFA0404503) and the National Science Foundation of China (grant No. 12073014). F.S. acknowledges support from the NRAO Student Observing Support (SOS) award SOSPA7-022. F.S. and E.E. acknowledge funding from JWST/NIRCam contract to the University of Arizona, NAS5-02105. F.E.B. acknowledges support from ANID-Chile BASAL CATA ACE210002 and FB210003, FONDECYT Regular 1200495 and 1190818, and Millennium Science Initiative Program—ICN12_009. F.W. is thankful for support provided by NASA through the NASA Hubble Fellowship grant No. HST-HF2-51448.001-A awarded by the Space Telescope Science Institute, which is operated by the Association of Universities for Research in Astronomy, Inc., under NASA contract NAS5-26555.

This work is based on observations made with the NASA/ESA/CSA James Webb Space Telescope. The data were obtained from the Mikulski Archive for Space Telescopes at the Space Telescope Science Institute, which is operated by the Association of Universities for Research in Astronomy, Inc., under NASA contract NAS 5-03127 for JWST. These observations are associated with program ERS-1324. The authors acknowledge the GLASS team for developing their observing program with a zero-exclusive-access period.

This paper makes use of the following ALMA data: ADS/JAO.ALMA#2017.1.01219.S. ALMA is a partnership of ESO (representing its member states), NSF (USA) and NINS (Japan), together with NRC (Canada), MOST and ASIAA (Taiwan), and KASI (Republic of Korea), in cooperation with the Republic of Chile. The Joint ALMA Observatory is operated by ESO, AUI/NRAO, and NAOJ. In addition, publications from NA authors must include the standard NRAO acknowledgment: The National Radio Astronomy Observatory is a facility of the National Science Foundation operated under cooperative agreement by Associated Universities, Inc.

This work is based on data and catalog products from Hubble Frontier Fields (HFF)-DeepSpace, funded by the National Science Foundation and Space Telescope Science Institute (operated by the Association of Universities for Research in Astronomy, Inc., under NASA contract NAS5-26555).

JWST data used in this paper were obtained from the Mikulski Archive for Space Telescopes (MAST) at the Space Telescope Science Institute. The specific observations analyzed can be accessed via doi:10.17909/91zv-yg35.

Facilities: JWST, ALMA, HST.

Software: astropy (Astropy Collaboration et al. 2022), `BAGPIPES` (Carnall et al. 2018), `EAZY` (Brammer et al. 2008), `Grizli` (Brammer 2022), `glafic` (Oguri 2010), `Qubefit` (Neeleman et al. 2020).

Appendix A
Tentative Foreground Contamination

In Figure 1, there is a white core near the center of A2744-DSG-z3. In this section, we discuss the possibility of contamination caused by a foreground cluster dwarf galaxy. We combined archival Hubble Space Telescope photometric observations and JWST/NIRISS grism data to reveal whether it is a foreground galaxy. Figure 5 shows these observations. We performed photometric measurements using an aperture with radius of $0\farcs5$ on the PSF-matched images obtained from the HFF-DeepSpace (Shipley et al. 2018; Nedkova et al. 2021). Based on SED-fitting results, the best-fit redshift of this target is $z = 0.422$ ($z = 0.544^{+0.006}_{-0.003}$) given by EAZY (GRIZLI). We conclude that from the photometric and grism data, this target could be a foreground contamination, despite that the redshift determination of this target is not secure.

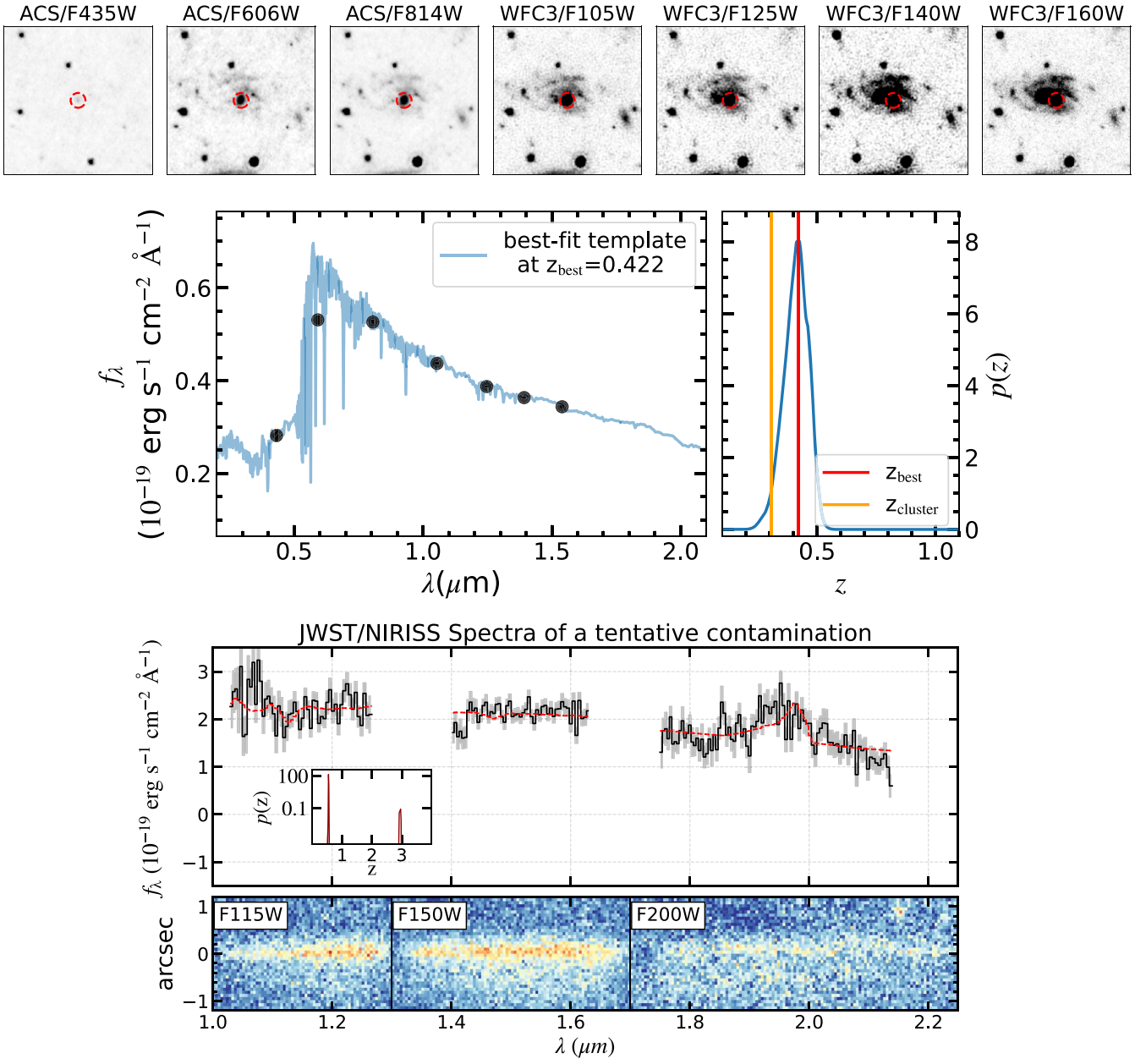

Figure 5. Top: seven-band HST observations. The red cycle indicates the location and apertures ($r = 0\farcs5$) used for this tentative foreground galaxy. Middle: photometric redshift solution based on EAZY. In the left panel, the best-fit SED is shown in blue. Meanwhile, in the right panel, the redshift probability distribution is shown in blue. The best-fit redshift ($z_{\rm best} = 0.422$) and the redshift of cluster A2744 are marked as red and orange lines, respectively. Bottom: 2D/1D JWST/NIRISS spectra of the tentative target. Each panel is the same as that in the right panel of Figure 2. We conclude that, from the grism spectra, we cannot directly determine the redshift of the tentative contamination because there are no obvious emission lines. The best-fit redshift obtain from GRIZLI is $z = 0.544^{+0.006}_{-0.003}$. However, there is still a high-redshift solution. Thus, we cannot rule out the possibility that this target is located at the same redshift of A2744-DSG-z3.

Appendix B
Mass-to-light Ratio versus Color Relation

Empirically, Bell & de Jong (2001) presented a strong correlation between stellar mass-to-light ($M_{\rm star}/L$) ratio and the optical colors for spiral galaxies. Therefore, the JWST rest-frame optical and high-spatial-resolution observations give us the first opportunity to resolve the stellar-mass distribution of a spiral galaxy at $z = 3.06$. To measure the pixelated stellar mass of A2744-DSG-z3, we follow the procedures in Lang et al. (2019). The $M_{\rm star}/L$ versus color relation is constructed and calibrated by synthetic galaxy SEDs.

To generate mocked SEDs, we use a public python package `BAGPIPES` (Carnall et al. 2018) by adopting different stellar parameters (e.g., the age/metallicity of stellar populations $t_{\rm age}/Z$, and the dust-attenuation parameter in the rest-frame V band, A_V). For galaxy models, we assume a Kroupa (2002) initial mass function with $t_{\rm age}$ ranging from 0.05 to 2 Gyr, while Z ranges from 0.4 to 2.5 $Z_{\odot}$. Then, we assume an exponentially declining star formation history (SFR) with timescales of $\tau_{\rm SFR} = 30$ Myr, which is guided by the best fitting result of a similar red spiral galaxy at $z \sim 2.5$ (Fudamoto et al. 2022). In order to convert these mocked galaxy SEDs to colors, we apply a Calzetti et al. (2000) dust-attenuation law with $A_V = 0.0$–2.0. Figure 6 shows the $M_{\rm star}/L$ versus color relation. We define the $M_{\rm star}/L$ as $(\log M_{\rm star} + 0.4K_{200})$, similar to that in Lang et al. (2019). The best-fit linear relation is $M_{\rm star}/L = 0.55 \times (J_{115} - K_{200}) + 18.92$.

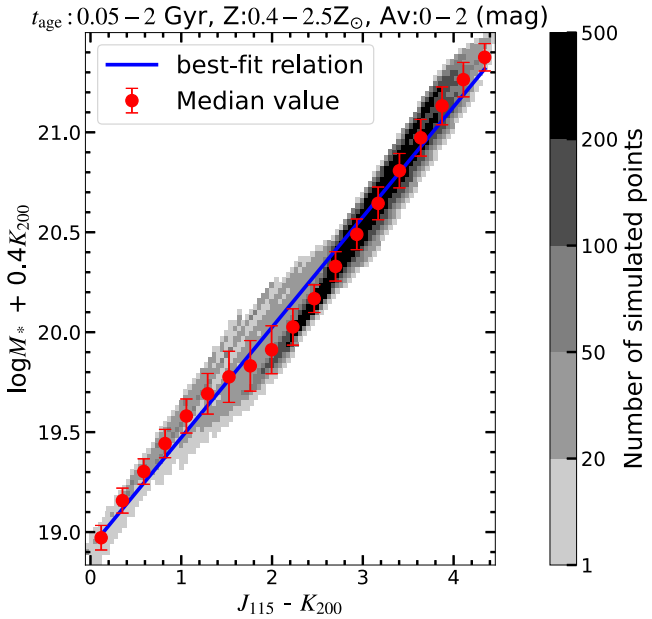

Figure 6. Simulated $M_{\rm star}/L$ vs. color relation. Grayscale images represents the number of simulated data points with different stellar parameters (e.g., $t_{\rm age}$, Z, and A_v). Stellar ages range from 50 Myr to 2 Gyr at $z = 3.06$, while metallicity ranges from 0.4 to 2.5 $Z_{\odot}$. The simulated colors are derived by adopting the Calzetti et al. (2000) law with $A_V = 0.0$–2.0 (mag). Red points are median values in different color bins, while error bars are standard deviations in each bin. The blue line is a best-fit linear relation using the median points.

Appendix C
CO Moment Maps

We extract the kinematic information from the CO data cubes by constructing velocity maps (mom-1) and velocity dispersion maps (mom-2). Here, we display the results in Figure 7. For A2744-DSG-z3, using the CASA task `imfit`, the CO intensity is marginally resolved with the deconvolved sizes of $1\farcs43 \times 0\farcs66$ and $1\farcs37 \times 0\farcs79$ for CO (5–4) and CO (3–2), respectively. This corresponds to a physical size of 4.5 kpc × 2.1 kpc and 4.3 kpc × 2.5 kpc at $z = 3.059$ (delensed). The measured size is slightly smaller than those of five star-forming galaxies with comparable mass at similar redshifts (Cassata et al. 2020). Moreover, the CO mom-1 maps show a tentatively rotating feature (the third-column two panels in Figure 7). The measured rotation velocity is about ∼200 km s^{-1} (inclination corrected).

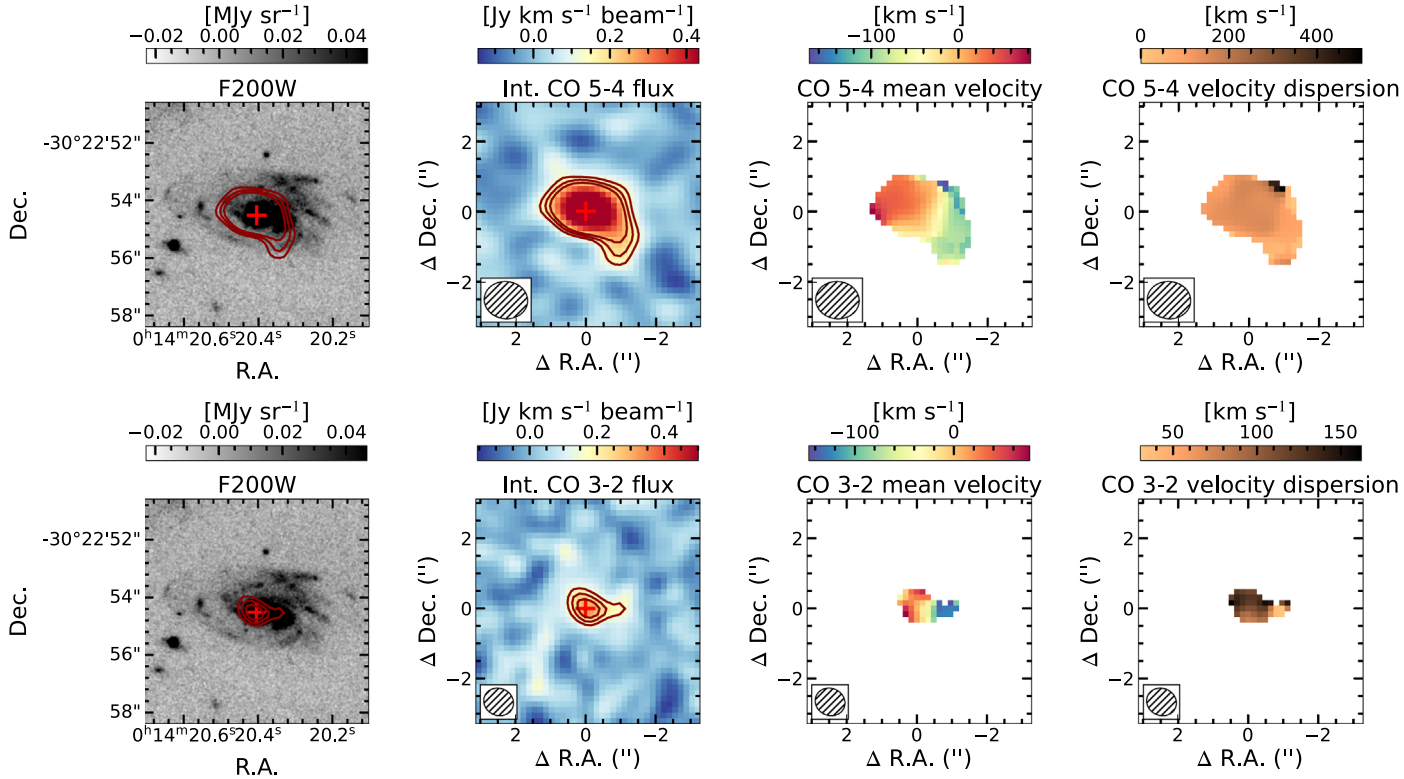

Figure 7. Left: JWST/NIRISS F200W observations, overlaid with contours of the CO lines (in dark red). The red cross represents the center of A2744-DSG-z3. Second to last column: CO flux density, velocity, and velocity dispersion. The synthesized beams are shown at the lower left corner of each panels with size of $1\farcs24 \times 1\farcs06$ (CO (5–4)) and $0\farcs86 \times 0\farcs77$ (CO (3–2)), respectively. The contours are drawn at [3, 4, 5] × 1σ. For mom-1 and mom-2 maps, regions with flux smaller than 2σ are masked.

ORCID iDs

Yunjing Wu https://orcid.org/0000-0003-0111-8249
Zheng Cai https://orcid.org/0000-0001-8467-6478
Fengwu Sun https://orcid.org/0000-0002-4622-6617
Fuyan Bian https://orcid.org/0000-0002-1620-0897
Xiaojing Lin https://orcid.org/0000-0001-6052-4234
Zihao Li https://orcid.org/0000-0001-5951-459X
Mingyu Li https://orcid.org/0000-0001-6251-649X
Franz E. Bauer https://orcid.org/0000-0002-8686-8737
Eiichi Egami https://orcid.org/0000-0003-1344-9475
Xiaohui Fan https://orcid.org/0000-0003-3310-0131
Jorge González-López https://orcid.org/0000-0003-3926-1411
Jianan Li https://orcid.org/0000-0002-1815-4839
Feige Wang https://orcid.org/0000-0002-7633-431X
Jinyi Yang https://orcid.org/0000-0001-5287-4242
Shiwu Zhang https://orcid.org/0000-0002-0427-9577
Siwei Zou https://orcid.org/0000-0002-3983-6484

References

Aravena, M., Boogaard, L., Gónzalez-López, J., et al. 2020, ApJ, 901, 79
Astropy Collaboration, Price-Whelan, A. M., Lim, P. L., et al. 2022, ApJ, 935, 167
Bell, E. F., & de Jong, R. S. 2001, ApJ, 550, 212
Bolatto, A. D., Wong, T., Utomo, D., et al. 2017, ApJ, 846, 159
Boyett, K., Mascia, S., Pentericci, L., et al. 2022, ApJL, 940, L52
Brammer, G. 2022, grizli, Version 1.6.0, Zenodo, doi:10.5281/zenodo.6985519
Brammer, G. B., van Dokkum, P. G., & Coppi, P. 2008, ApJ, 686, 1503
Calzetti, D., Armus, L., Bohlin, R. C., et al. 2000, ApJ, 533, 682
Carnall, A. C., McLure, R. J., Dunlop, J. S., & Dave, R. 2018, MNRAS, 480, 4379
Cassata, P., Liu, D., Groves, B., et al. 2020, ApJ, 891, 83
Cen, R. 2014, ApJL, 789, L21
Chen, C.-C., Gao, Z.-K., Hsu, Q.-N., et al. 2022, ApJL, 939, L7
Chen, Y., Steidel, C. C., Erb, D. K., et al. 2021, MNRAS, 508, 19
Conselice, C. J. 2014, ARA&A, 52, 291
Conselice, C. J., Blackburne, J. A., & Papovich, C. 2005, ApJ, 620, 564
Davis, B. L., Berrier, J. C., Shields, D. W., et al. 2012, ApJS, 199, 33
Dawson, S., McCrady, N., Stern, D., et al. 2003, AJ, 125, 1236
Elmegreen, B. G. 2002, ApJ, 577, 206
Elmegreen, B. G., Elmegreen, D. M., Fernandez, M. X., & Lemonias, J. J. 2009, ApJ, 692, 12
Elmegreen, D. M., & Elmegreen, B. G. 2014, ApJ, 781, 11
Elmegreen, D. M., Elmegreen, B. G., Yau, A., et al. 2011, ApJ, 737, 32
Fiacconi, D., Feldmann, R., & Mayer, L. 2015, MNRAS, 446, 1957
Flewelling, H. A., Magnier, E. A., Chambers, K. C., et al. 2020, ApJS, 251, 7
Fudamoto, Y., Inoue, A. K., & Sugahara, Y. 2022, ApJL, 938, L24
Gaia Collaboration, Prusti, T., de Bruijne, J. H. J., et al. 2016, A&A, 595, A1
Gaia Collaboration, Vallenari, A., Brown, A. G. A., et al. 2022, arXiv:2208.00211
Genzel, R., Price, S. H., Übler, H., et al. 2020, ApJ, 902, 98
Gómez-Guijarro, C., Elbaz, D., Xiao, M., et al. 2022, A&A, 658, A43
González-López, J., Bauer, F. E., Romero-Cañizales, C., et al. 2017, A&A, 597, A41
Gullberg, B., Smail, I., Swinbank, A. M., et al. 2019, MNRAS, 490, 4956
Hammer, F., Flores, H., Puech, M., et al. 2009, A&A, 507, 1313
Hodge, J. A., Swinbank, A. M., Simpson, J. M., et al. 2016, ApJ, 833, 103
Hunt, L. K., Draine, B. T., Bianchi, S., et al. 2015, A&A, 576, A33
Kohandel, M., Pallottini, A., Ferrara, A., et al. 2019, MNRAS, 487, 3007
Krabbe, A. C., Pastoriza, M. G., Winge, C., et al. 2011, MNRAS, 416, 38
Kroupa, P. 2002, Sci, 295, 82
Lang, P., Schinnerer, E., Smail, I., et al. 2019, ApJ, 879, 54
Laporte, N., Bauer, F. E., Troncoso-Iribarren, P., et al. 2017, A&A, 604, A132
Law, D. R., Shapley, A. E., Steidel, C. C., et al. 2012, Natur, 487, 338
Law, D. R., Steidel, C. C., Erb, D. K., et al. 2009, ApJ, 697, 2057
Li, Z., Wang, X., Cai, Z., et al. 2022, ApJL, 929, L8
Lin, C. C., & Shu, F. H. 1964, ApJ, 140, 646
Madau, P., & Dickinson, M. 2014, ARA&A, 52, 415
Margalef-Bentabol, B., Conselice, C. J., Haeussler, B., et al. 2022, MNRAS, 511, 1502
McMullin, J. P., Waters, B., Schiebel, D., Young, W., & Golap, K. 2007, in ASP Conf. Ser. 376, Astronomical Data Analysis Software and Systems XVI, ed. R. A. Shaw, F. Hill, & D. J. Bell (San Francisco, CA: ASP), 127
Moore, T. J. T., Urquhart, J. S., Morgan, L. K., & Thompson, M. A. 2012, MNRAS, 426, 701
Nedkova, K. V., Häußler, B., Marchesini, D., et al. 2021, MNRAS, 506, 928
Neeleman, M., Prochaska, J. X., Kanekar, N., & Rafelski, M. 2020, qubefit: MCMC Kinematic Modeling, Astrophysics Source Code Library, ascl:2005.013
Nelson, E. J., van Dokkum, P. G., Forster Schreiber, N. M., et al. 2016, ApJ, 828, 27
Oguri, M. 2010, glafic: Software Package for Analyzing Gravitational Lensing, Astrophysics Source Code Library, ascl:1010.012
Rigby, J., Perrin, M., McElwain, M., et al. 2022, arXiv:2207.05632
Rodríguez-Puebla, A., Primack, J. R., Avila-Reese, V., & Faber, S. M. 2017, MNRAS, 470, 651
Schlawin, E., Leisenring, J., Misselt, K., et al. 2020, AJ, 160, 231
Shipley, H. V., Lange-Vagle, D., Marchesini, D., et al. 2018, ApJS, 235, 14
Somerville, R. S., Behroozi, P., Pandya, V., et al. 2018, MNRAS, 473, 2714
Speagle, J. S., Steinhardt, C. L., Capak, P. L., & Silverman, J. D. 2014, ApJS, 214, 15
Sun, F., Egami, E., Fujimoto, S., et al. 2022, ApJ, 932, 77
Sun, F., Egami, E., Rawle, T. D., et al. 2021, ApJ, 908, 192
Tacchella, S., Dekel, A., Carollo, C. M., et al. 2016, MNRAS, 457, 2790
Tadaki, K.-i., Belli, S., Burkert, A., et al. 2020, ApJ, 901, 74
Tadaki, K.-i., Genzel, R., Kodama, T., et al. 2017, ApJ, 834, 135
Treu, T., Roberts-Borsani, G., Bradac, M., et al. 2022, ApJ, 935, 110
Tsukui, T., & Iguchi, S. 2021, Sci, 372, 1201
Wang, X., Jones, T., Vulcani, B., et al. 2022, ApJ, 938, L16
Wuyts, S., Förster Schreiber, N. M., Genzel, R., et al. 2012, ApJ, 753, 114